BIOMIMETIC FLOW IMAGING WITH AN ARTIFICIAL FISH LATERAL LINE

Nam Nguyen, Douglas Jones

Coordinated Science Laboratory, University of Illinois, Urbana Champaign, USA

Saunvit Pandya, Yingchen Yang, Nannan Chen, Craig Tucker, Chang Liu

Micro and Nanotechnology Laboratory, University of Illinois, Urbana Champaign, USA

Keywords: Artificial lateral line, flow imaging, MEMS sensor array, calibration, adaptive beamforming, Capon beamforming, Cramer-Rao Lower Bound.

Abstract: Almost all fish possess a flow-sensing system along their body, called the lateral line, that allows them to perform various behaviours such as schooling, preying, and obstacle or predator avoidance. Inspired from this, our group has built artificial lateral lines from newly-developed flow sensors using Micro-Electro-Mechanical Systems (MEMS) technology. To make our lateral line a functional sensory system, we develop an adaptive beamforming algorithm (applying Capon's method) that provides our lateral line with the capability of imaging the locations of oscillating dipoles in a 3D underwater environment. To help our sensor arrays adapt to the environment for better performance, we introduce a self-calibration algorithm that significantly improves the image accuracy. Finally, we derive the Cramer-Rao Lower Bound (CRLB) that represents the fundamental perfomance limit of our system and provides guidance in optimizing artificial lateral-line systems.

1 INTRODUCTION

Biologists have discovered that almost all species of fish have a flow-sensing system, called the lateral line, consisting of cilium-like haircell sensors (Figure 1) (Dijkgraaf, 1963). Each haircell sensor in the lateral line measures local fluid flow velocity, and fish rely on their lateral lines to perform a wide range of activities including schooling, preying, navigation, and predator avoidance (Pitcher and Wardle, 1976; Coombs, 1994). Studies show that using its lateral lines, a fish can locate and track an acoustic dipole source (Coombs and Conley, 1997), which models the back-and-forth motion of the tail of smaller prey or other fish.

Inspired by the capability of the fish lateral lines, we are developing an equivalent engineered system, an artificial lateral line. Potential applications include maneuvering Autonomous Underwater Vehicles (AUV), dynamic imaging in an underwater environment, detecting corrosion or leaks inside pipes, and detecting and tracking intruders such as swimmers or submarines.
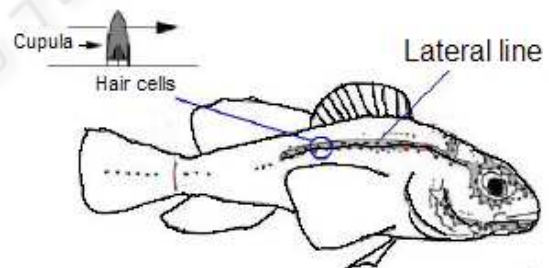
Recent advances in Micro-Electro-Mechanical

Figure 1: Hair cell sensor system in fish.

Systems (MEMS) technology make it possible to build micrometer-scale sensors mimicking the function and structure of fish lateral lines. The first MEMS lateral line consists of a linear array of 16 hotwire amemometers (Fan et al., 2002). These sensors are capable of measuring flow magnitude but not direction. Recently, MEMS haircell flow sensors, which are sensitive to flow direction, have also been developed (Chen and Liu, 2003).

Along with development of sensors, signal-processing algorithms are also required to make a complete artificial lateral-line sensory system. Pre-

vious work in this area localizes and tracks an acoustic source using a ML estimator (Pandya et al., 2006) and introduces a new method for imaging all flow sources surrounding a sensor array (Pandya et al., 2007). In this paper, we extend the work in (Pandya et al., 2007) to cover mapping in three-dimentional space (3D imaging). In particular, we review the dipole model and modify the beamforming algorithm in (Pandya et al., 2007) to handle 3D imaging of dipoles using haircell sensors. Next, we present a self-calibration algorithm to adjust the gains across the sensors to improve estimation accuracy. Finally, we derive the Cramer-Rao Lower Bound (CRLB) for the dipole position estimate to find the fundamental performance limits of the system.

2 ARTIFICIAL LATERAL-LINE SENSORS

We have used three types of flow sensors to build artificial lateral lines: conventional hot-wire sensors, micromachined (MEMS) hot-wire sensors, and hair-cell sensors (Figure 2). Both types of hot-wire sensors operate on the heat dissipation principle. Voltage applied across a sensor heats up the wire. Movement of water or air particles across the hot wire carries away heat causing a change in the wire's resistance and in turn the current. The change in current reflects the speed of water or air particles moving across the wire.
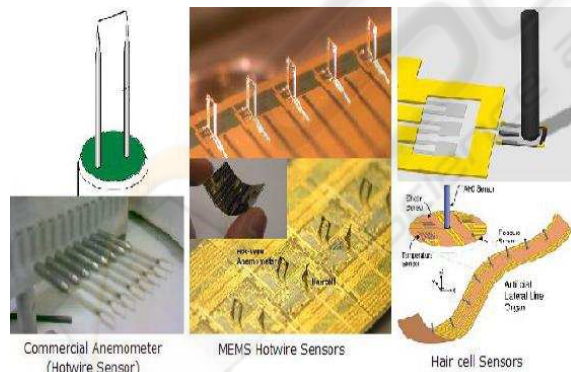

Figure 2: Three types of flow sensors for underwater acoustic signals.

Conventional hotwire sensors are bulky and costly. This makes it hard to form small and dense arrays of sensors for artificial lateral lines. To overcome those drawbacks, micromachined hotwire sensors have been developed (Chen et al., 2003). They can be integrated to form a lateral line in a canal as

in fish or to form a dense array of sensors with 1mm spacing . However, the sensors are fragile and cannot distinguish the direction of flow. To avoid these problems, micromachined haircell sensors were invented that operate on the same principle as in fish. The hair of the sensor intercepts the flow, and the force applied on the hair is transformed into stress at the base of the hair. A piezo-electric strain gauge on a cantilever at the base translates the stress into an electronic signal (Yang et al., 2007). The advantages of the haircell sensors are robustness and directional sensing capability.

3 FLOW IMAGING USING A BEAMFORMING APPROACH

Our main goal is to estimate the locations of dipole sources using arrays of flow sensors in an underwater environment. In our laboratory experiment, the dipole source is a small sphere oscillating back and forth in a certain direction at a fixed frequency. We start with a dipole source since it is simple enough so that its surrounding flow field model is well established. Moreover, dipole-like flow sources are commonly encountered in nature, such as the waving tail of a fish. Biologists have extensively studied fish lateral-line response to acoustic dipoles and found that fish can locate the source of a dipole and track its movement, and at least some species treat it as prey (Coombs, 1994).

A model of an oscillating dipole source in fluid has been well studied in (Coombs, 2003). The flow velocity at a point in space near a dipole source is modeled as

$$\vec{v}_{flow}(r,\theta) = \left(a^3 U_o \frac{\cos(\theta)}{r^3} \right) \hat{\mathbf{r}} + \left(\frac{a^3 U_o}{2} \frac{\sin(\theta)}{r^3} \right) \hat{\theta}. \tag{1}$$

In the above equation, the flow velocity is a function of the dipole diameter a, the initial vibrational velocity amplitude U_o, and the observation distance r and angle θ as shown in Figure 3a. Also, $\hat{\mathbf{r}}$ and $\hat{\theta}$ are unit vectors of the dipole's spherical coordinates at the sensor's position.

The flow velocity in Equation (1) is, however, derived in the dipole's spherical coordinates. It is more convenient to compute flow velocity in the fish's Cartesian coordinates (Figure 3b) so that we can derive array patterns due to a dipole oscillating in a certain direction at some location in space. Transformed into the fish's Cartesian coordinates, the flow velocity is then

$$\vec{v}_{flow}(\vec{s}) = \frac{a^3 U_o}{2r^3} \left(3\cos(\theta)\hat{\mathbf{r}} - \hat{\mathbf{z}}_d \right) \tag{2}$$
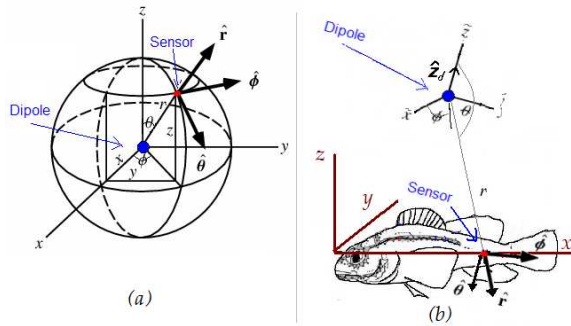
Figure 3: (a) Dipole's Spherical coodinates. (b) Fish's Cartesian coordinates.

where $\hat{\mathbf{z}}_d$ is now the unit vector on the oscillating axis of the dipole and $\vec{s} = (x_s, y_s, z_s)$ is the vector representing the position of the sensor in the fish's coordinates. If $\vec{d} = (x_d, y_d, z_d)$ is the vector that indicates the position of the dipole, then

$$r = \|\vec{s} - \vec{d}\| \text{ and } \hat{\mathbf{r}} = \frac{\vec{s} - \vec{d}}{\|\vec{s} - \vec{d}\|}$$

Researchers have studied how the lateral lines in fish respond to the fluid-flow field created by a dipole source. In (Curcic-Blake and van Netten, 2006), the excitation patterns along the lateral line of a ruffle fish (*Gymnocephalus cernuus* L.) were electrophysiologically measured, then compared to theoretical predictions and found to be in good agreement. The authors also applied a continuous wavelet transform (CWT) algorithm on the collected signals to produce a 2D-contour map of the area surrounding the dipole source. Although the region of the dipole source can be identified from the contour map, the map has poor resolution, making it difficult to visually locate the dipole's position or to see multiple simultaneous sources.

Approaching this problem from the engineering side, our research group has implemented artificial lateral lines with both conventional and MEMS hotwire sensors and used them to capture the signals in the flow field created by a dipole source. An adaptive beamforming approach using Capon's beamformer (Capon, 1969) yielded a much higher resolution spatial imaging of dipole source then the CWT (Pandya et al., 2007).

(Curcic-Blake and van Netten, 2006) and (Pandya et al., 2007) only focus on the case of two-dimensional imaging. That means that the dipole source and all the sensors are in the *XY*-plane, and the estimation is only concerned with the *x* and *y* coordinates. Moreover, (Pandya et al., 2007) used hotwire sensors that measure flow magnitude, not flow direction. In this case, the dipole model in Equation (2)

reduces to

$$
\begin{aligned}
\|\vec{v}_{flow}(\vec{s})\| &= \frac{a^3 U_o}{2r^3} \|3\cos(\theta)\hat{\mathbf{r}} - \hat{\mathbf{z}}_d\| \\
&= \frac{a^3 U_o}{2r^3} \sqrt{3\cos^2(\theta) + 1}. \quad (3)
\end{aligned}
$$

In fact, Equation (3) is simplified further when the dipole's direction of oscillating $\hat{\mathbf{z}}_d$ is perpendicular to *XY*-plane

$$\|\vec{v}_{flow}(\vec{s})\| = \frac{a^3 U_o}{2r^3} \text{ since } \theta = \pi/2. \quad (4)$$

Equation (4) is used in (Pandya et al., 2007) to compute expected sensor readings for each position of dipole in the grid. However, this model no longer holds when we extend the problem to 3D imaging using haircell flow sensors.

3.1 3D Imaging with Haircell Sensors

Figure 4 illustrates how the flow velocity $\vec{v}_{flow}$ impacts on the hair of an artificial hair cell (AHC) sensor. A dipole source is located above the sensor in 3D space. The flow velocity is computed using Equation (2). Note that flow velocity now can be in any direction in 3D space. We neglect here any effects introduced by the structure to which the sensors are attached. Figure 4a shows the side view of the flow vector and Figure 4b shows the top view of it.
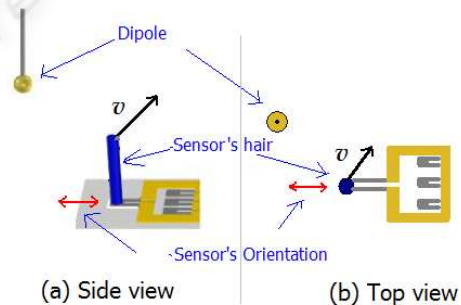

Figure 4: (a) Side view of sensor and dipole. (b) Top view of sensor and dipole.

A single AHC sensor can only measure flow parallel with the strain-guage cantilever. Therefore, an AHC sensor does not measure the magnitude and direction of the flow velocity $\vec{v}_{flow}$ but measures the projection of the flow velocity onto the sensor's orientation axis. The sensors' orientations are thus essential information to determine the sensor array response.

We extend the adaptive beamforming algorithm in (Pandya et al., 2007) to enable 3D imaging with AHC sensors via the steps summarized below:

- Step 1: Compute the expected sensor array pattern for each dipole position (x_d, y_d, z_d) in the 3D grid. For each sensor in the array, use Equation (2) to compute the flow velocity at that sensor, and then project the flow velocity onto the sensor's orientation axis. This produces a template of the array pattern including L sensor readings

$$\mathbf{s}_{(x_d, y_d, z_d)} = [s_1, s_2, \ldots, s_L].$$

Note that the flow velocity in Equation (2) is determined by the sensor position vector $\vec{s}$, the dipole position vector $\vec{d} = (x_d, y_d, z_d)$, and the dipole oscillating vector $\hat{\mathbf{z}}_d$. $\hat{\mathbf{z}}_d$ is a unit vector defined by the azimuth angle θ_d and the zenith angle ϕ_d. So there are in total 5 parameters to define a dipole, namely x_d, y_d, z_d for position and θ_d, ϕ_d for oscillating direction.

- Step 2: Compute the outer-product from the sensor samples

$$\mathbf{R} = \frac{1}{N} \sum_{n=1}^{N} \mathbf{x}[n] * \mathbf{x}^T[n]$$

where $\mathbf{x}[n]$ is the discrete-time vector of samples of the collected signals.

- Step 3: Using Capon's method, compute the energy level at each point in the grid

$$E = \frac{1}{\mathbf{s}_{\vec{d}}^H \mathbf{R}^{-1} \mathbf{s}_{\vec{d}}}$$

- Step 4: Plot a map of energy level E for each point in the 3D grid. The high-energy regions in the map correspond to the dipole sources' locations.
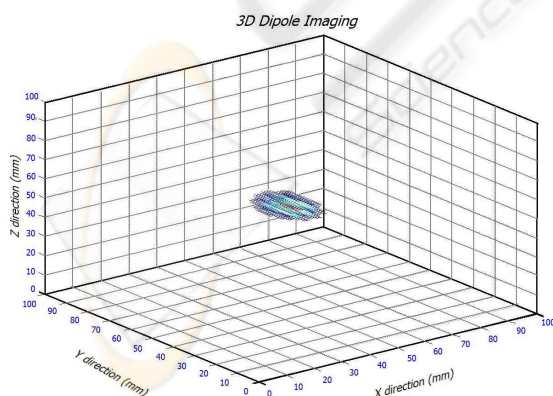

Figure 5: 3D Dipole Imaging with a dipole oscillating at (50,50,50).

The above algorithm is used in a 3D dipole imaging simulation, and the results are shown in Figure 5.

In this case, we simulate 2 arrays in an L-shape pattern with a total of 21 haircell sensors on the x and z axes. On each of two axes, there are 11 sensors spaced 10 mm apart from 0 to 100 mm. A dipole is located at $(50, 50, 50)$. Figure 5 shows a sphere centered around the dipole source with different colour intensity. High intensity presents the energy level output (from Capon's formula) at the local point. That means the dipole is most likely there.

4 SELF-CALIBRATION ALGORITHM

Calibration of sensors is an important practical step before doing any signal analysis. Since each individual sensor's sensitivity gain can vary (especially for sensors still in the laboratory stage of development), poor calibration will lead to poor estimation performance. Biological systems have a remarkable ability to tune their response to environmental variation, growth, or injury. Self-tuning ability is equally desirable for an engineered system. In this section, we propose an effective way of doing sensor array calibration for this type of experiment.

A straightforward method for calibration of a sensor array is to sequentially place a dipole in front of each sensor in the array, then record readings of all the sensors, which form a series of array patterns. Ideally, all the patterns should have similar shape and magnitude with the peak at the sensor closest to the dipole. However, measured array patterns vary significantly due to the non-uniformity of sensor gains. Figure 6 displays an example of the measured array patterns before calibration.
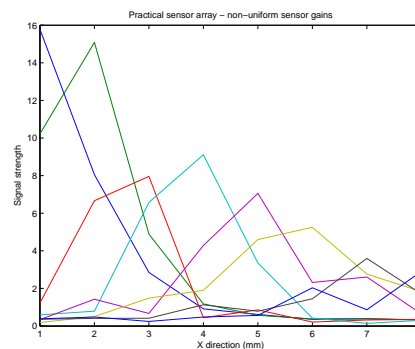

Figure 6: Measured sensor array patterns (non-uniform sensor gains).

Mathematically, the calibration problem can be formulated as follows. Consider a linear array of L evenly spaced sensors and a series of measurements

as the dipole travels a linear path at a constant distance from the sensor array. When the dipole is in front of Sensor 1, the ideal array pattern will be

$$[s_0, s_1, s_2, \ldots, s_{L-1}]$$

at Sensor 2, it will be $[s_{-1}, s_0, s_1, \ldots, s_{L-2}]$ and so on until sensor L, $[s_{-L+1}, s_{-L+2}, \ldots, s_0]$. Stacking those ideal array patterns together produces a Toeplitz matrix

$$A = \begin{bmatrix} s_0 & s_1 & s_2 & \cdots & \cdots & s_{L-1} \\ s_{-1} & s_0 & s_1 & \ddots & & s_{L-2} \\ s_{-2} & s_{-1} & \ddots & \ddots & \ddots & \vdots \\ \vdots & \ddots & \ddots & \ddots & s_1 & s_2 \\ \vdots & & \ddots & s_{-1} & s_0 & s_1 \\ s_{-(L-1)} & \cdots & \cdots & s_{-2} & s_{-1} & s_0 \end{bmatrix}$$

As each sensor i has a gain g_i, the matrix of array patterns with gains is

$$B = \begin{bmatrix} g_1 s_0 & g_2 s_1 & g_3 s_2 & \cdots & g_L s_{L-1} \\ g_1 s_{-1} & g_2 s_0 & g_3 s_1 & \ddots & g_L s_{L-2} \\ g_1 s_{-2} & g_2 s_{-1} & \ddots & \ddots & \vdots \\ \vdots & \ddots & \ddots & \ddots & g_L s_2 \\ \vdots & & \ddots & g_{(L-1)} s_0 & g_L s_1 \\ g_1 s_{-(L-1)} & \cdots & \cdots & g_{(L-1)} s_{-1} & g_L s_0 \end{bmatrix}$$

With noise included, the actual readings may be $C = B + N$, where C is the noisy version of B. Figure 6 shows the measured array patterns by plotting the rows of the matrix C. Although each pattern seems to have the peak at the sensor closest to the dipole, the shapes of the patterns are quite different due to non-uniform sensor gains. The aim of calibration is to find a set of sensor gains $[g_1, g_2, \ldots, g_L]$ and matrix A that approximate C as closely, as possible, i.e.

$$A * \begin{bmatrix} g_1 & 0 & \cdots & 0 \\ 0 & g_2 & \ddots & 0 \\ \vdots & & \ddots & \vdots \\ 0 & \cdots & 0 & g_L \end{bmatrix} \approx C$$

This is a bilinear least squares problem, which is a simple special case of a mixed linear-nonlinear least squares problem (Golub and Pereyra, 1973). Golub and Pereyra (Golub and Pereyra, 1973) show that the optimal linear coefficients in the globally optimal solution are simply the linear least-squares solution when the nonlinear coefficients are fixed at their globally optimum values; since the bilinear form is linear in both the sensor gains g_i and the shift-invariant

dipole response pattern s_j when the other is held constant, this holds for both.

We apply the standard iterative solution approach in which we fix one set of coefficients, find the least-square optimal solution best fitting the measured data for the other, and iterate until convergence. (See, for example, (Bai and Liu, 2006) for recent convergence theorems for this algorithm for random inputs.) The algorithm is as follows:

- Step 1: Initialize with uniform gains $g_1 = g_2 = \ldots = g_L = 1$.

- Step 2: Fix the gains $[g_1, g_2, \ldots, g_L]$ and find the optimal least squares solution for the dipole response $[s_{(-L+1)}, s_{(-L+2)}, \ldots, s_0, \ldots, s_{(L-1)}]$. This is equivalent to summing matrix C diagonally and then dividing it by the sum of all gains corresponding to the column that the diagonal line crosses.

- Step 3: Fix the dipole response $[s_{(-L+1)}, s_{(-L+2)}, \ldots, s_0, \ldots, s_{(L-1)}]$ and find the optimal least squares solution for the gains $[g_1, g_2, \ldots, g_L]$. This is equivalent to summing up each column of C and dividing it by the sum of corresponding s_l that appeared in that column (see matrix B). For example, after summing up column 2, it is divided by the sum $(s_1 + s_0 + s_{-1} + \ldots + s_{(2-L)})$ to get g_2.

- Step 4: Go back to Step 2 with the new gains in Step 3. Repeat the process until convergence.

This method allows the on-line calibration of sensors from observation of a dipole source as it travels across the array. This can be exploited to develop a fully self-tuning system like biological systems.

Using the algorithm above, we show the improved results in Figure 7, using an array of 8 hotwire sensors positioned 12.5mm apart on the X-axis from 12.5mm to 100mm. A dipole is placed in front of each sensor and data are collected. Figure 7(A) displays the array patterns for these eight positions. As can be seen, these patterns do not look like a shifted version of each other. The calibration algorithm is applied to these patterns to produce the calibrated patterns in Figure 7(B). The improvement in the magnitude and shape of those patterns is clear. The effect of the calibration algorithm can be clearly seen as we run a 2D imaging test of estimating the location of a dipole located in front of sensor 4 (50 mm). The image in Figure 7(C) is the result of processing signals without calibration while the one in Figure 7(D) uses calibration. There is obviously a significant improvement in the accuracy of the image produced by using calibration.
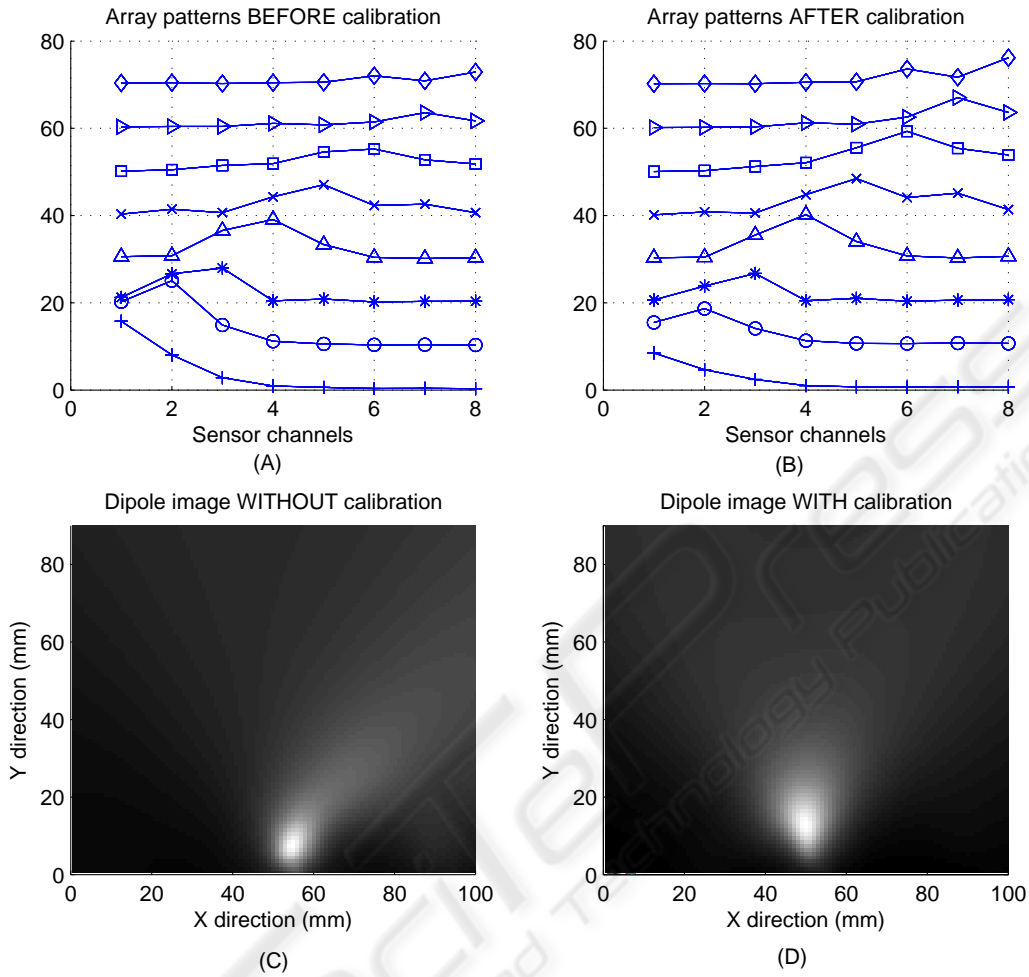
Figure 7: Effects of Self-calibration: (A) Measured array patterns (before calibration), (B) Calibrated array patterns, (C) 2D dipole imaging without calibration, (D) 2D dipole imaging with calibration.

5 CRAMER-RAO BOUND ON DIPOLE LOCALIZATION

Fundamental lower bounds on the error of the dipole position estimate for lateral-line sensors are very useful for evaluation of the estimator presented in Section 3.1, for finding the fundamental performance limit of a lateral line array, and for evaluating different sensor array configurations.

The signal captured by sensor k can be modeled as

$$s_k = f_k(\vec{d}) + N_k \tag{5}$$

where N_k is the additive Gaussian noise and $f_k(\vec{d})$ is the expected reading at sensor k produced by a dipole at location $\vec{d}$. For the case of 2D imaging ($\vec{d} = (x_d, y_d)$) using hotwire sensors, $f_k(\vec{d})$ is actually

computed by Equation (3); i.e., $f_k(\vec{d}) = \|\vec{v}_{flow}(\vec{s}_k)\|$. For case of 3D imaging using AHC sensors, $f_k(\vec{d})$ is computed as described in Step 1 of the algorithm in Section 3.1.

If the noises at all sensors are assumed to be i.i.d. with zero mean and variance σ_N^2, the signal vector of the sensor array $\mathbf{s}$ is a Gaussian random vector $\mathcal{N}(\mathbf{f}(\vec{d}), \mathbf{I}\sigma_N^2)$. Using the standard procedure in (Poor, 1988), we can derive the Fisher Information Matrix for the case of 2D imaging as

$$\mathbf{F} = \frac{1}{\sigma_N^2} \left[\begin{array}{cc} \sum_{k=1}^{L} \left(\frac{\partial f_k(x,y)}{\partial x} \right)^2 & \sum_{k=1}^{L} \frac{\partial f_k(x,y)}{\partial x} \frac{\partial f_k(x,y)}{\partial y} \\ \sum_{k=1}^{L} \frac{\partial f_k(x,y)}{\partial x} \frac{\partial f_k(x,y)}{\partial y} & \sum_{k=1}^{L} \left(\frac{\partial f_k(x,y)}{\partial y} \right)^2 \end{array} \right] \tag{6}$$

then the CRLB is

$$Var[\vec{d}] \geq [\mathbf{F}]^{-1} \tag{7}$$

For the case of 2D imaging using hotwire sensors as in (Pandya et al., 2007), we have from Equation (3)

$$f_k(x,y) = \frac{a^3 U_o}{2r^3} = \frac{a^3 U_o}{2\|\vec{s}_k - \vec{d}\|^3}$$
$$= \frac{a^3 U_o}{2[(x - x_{s_k})^2 + (y - y_{s_k})^2]^{\frac{3}{2}}}$$

then (6) becomes

$$\mathbf{F} = \frac{(\frac{3}{2} a^3 U_o)^2}{\sigma_N^2} \times$$

$$\begin{bmatrix} \sum_{k=1}^{L} \frac{(x - x_{s_k})^2}{[(x - x_{s_k})^2 + (y - y_{s_k})^2]^5} & \sum_{k=1}^{L} \frac{(x - x_{s_k})(y - y_{s_k})}{[(x - x_{s_k})^2 + (y - y_{s_k})^2]^5} \\ \sum_{k=1}^{L} \frac{(x - x_{s_k})(y - y_{s_k})}{[(x - x_{s_k})^2 + (y - y_{s_k})^2]^5} & \sum_{k=1}^{L} \frac{(y - y_{s_k})^2}{[(x - x_{s_k})^2 + (y - y_{s_k})^2]^5} \end{bmatrix}$$
(8)

We now compute the CRLB in Equation (8) for a system consisting of 16 hotwire sensors placed 6mm apart along the X-axis starting from 60mm to 90mm. The bounds on the estimation error's variance are represented by error ellipses in Figure 8. Each ellipse corresponds to a dipole located at its center. Note that the size of the ellipses grows larger as the dipole moves away from the array. This just agrees with the fact that as the dipole moves away from the sensor array, not only do the signals become weaker but also the array patterns flatten out. The CRLB shows that no signal processing algorithm can accurately estimate the location of dipoles at long range (more than about an array length) because the signals collected by sensors show almost no difference between dipole locations.

As the results show, the CLRB can be a source of design criteria to build a flow sensor array meeting requirements of image resolution and coverage range.

6 CONCLUSIONS

The adaptive beamforming approach to flow-field imaging can be generalized to produce an image of oscciliating dipoles' locations in a three-dimensional underwater environment. The images' accuracy increases significantly when a self-calibration algorithm to tune the sensors' gains is applied. The calibration algorithm, which uses the bilinear least squares technique, is a good starting point to build a system with the self-tuning capability that biological systems always exhibit. Our final result, the Cramer-Rao Lower Bound, is a useful tool to evaluate the performance limits of a lateral line system. This helps in the design of a better system. The bounds also confirm that a lateral-line system is neccessarily a near-field sense.
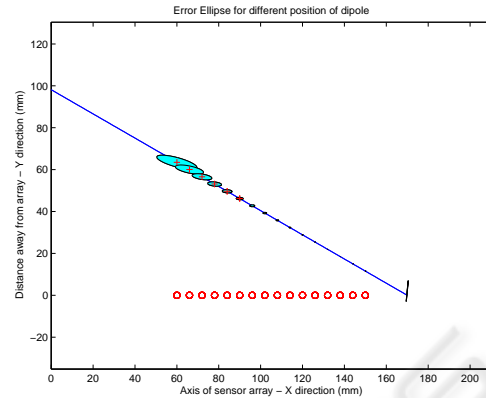

Figure 8: Error ellipse centered around different dipole positions, 16 sensors (the circles) are on the x-axis.

ACKNOWLEDGEMENTS

REFERENCES

Bai, E. and Liu, Y. (2006). Least squares solutions of bilinear equations. *Systems & Control Letters*, 55(6):466–472.

Capon, J. (1969). High-resolution frequency-wavenumber spectrum analysis. *Proceedings of the IEEE*, 57(8):1408–1418.

Chen, J., Fan, Z., Zou, J., Engel, J., and Liu, C. (2003). Two-dimensional micromachined flow sensor array for fluid mechanics studies. *Journal of Aerospace Engineering*, 16:85.

Chen, J. and Liu, J. (2003). Development of polymer-based artificial haircell using surface micromachining and 3D assembly. *TRANSDUCERS, Solid-State Sensors, Actuators and Microsystems, 12th International Conference on, 2003*, 2.

Coombs, S. (1994). Nearfield detection of dipole sources by the Goldfish (CARASSIUS AURATUS) and the Mottled Sculpin (COTTUS BAIRDI). *Journal of Experimental Biology*, 190:109–129.

Coombs, S. (2003). Dipole 3d user guide. Technical report.

Coombs, S. and Conley, R. (1997). Dipole source localization by mottled sculpin. I-III. *Journal of Comparative Physiology A: Sensory, Neural, and Behavioral Physiology*, 180(4):387–399.

Curcic-Blake, B. and van Netten, S. (2006). Source location encoding in the fish lateral line canal. *Journal of Experimental Biology*, 209(8):1548–1559.

Dijkgraaf, S. (1963). The functioning and significance of lateral-line organs. *Biology Review*, 38:51–105.

Fan, Z., Chen, J., Zou, J., Bullen, D., Liu, C., and Del-comyn, F. (2002). Design and fabrication of artificial lateral line flow sensors. *Journal of Micromechanics and Microengineering*, 12(5):655–661.

Golub, G. and Pereyra, V. (1973). The differentiation of pseudo-inverses and nonlinear least squares problems whose variables separate. *SIAM Journal on Numerical Analysis*, 10(2):413–432.

Pandya, S., Yang, Y., Jones, D., Engel, J., and Liu, C. (2006). Multisensor processing algorithms for under-water dipole localization and tracking using MEMS artificial lateral-line sensors. *EURASIP Journal on Applied Signal Processing*.

Pandya, S., Yang, Y., Liu, C., and Jones, D. (2007). Biomimetic imaging of flow phenomena. *Proceeding of Acoustics, Speech and Signal Processing, 2007. ICASSP 2007*, 2:II–933 – II–936.

Pitcher, T. Patridge, B. and Wardle, C. (1976). A blind fish can school. *Science*, 194:963–965.

Poor, V. (1988). *An Introduction to Signal Detection and Estimation*. Springer-Verlag.

Yang, Y., Chen, N., Tucker, C., Engel, J., Pandya, S., and Liu, C. (2007). From artificial haircell sensor to artificial lateral line system: development and application. *MEMS 2007 20th IEEE International Conference on Micro Electro Mechanical Systems, Kobe, Japan*.